Draft version September 2, 2023
Typeset using LaTeX **twocolumn** style in AASTeX631

Fossil Signatures of Main-sequence Convective Core Overshoot in Subgiant Stars Estimated through Asteroseismic Analyses

Christopher J. Lindsay [1] J. M. Joel Ong [2, 3] and Sarbani Basu [1]

[1] *Department of Astronomy, Yale University, PO Box 208101, New Haven, CT 06520-8101, USA*
[2] *Institute for Astronomy, University of Hawai'i, 2680 Woodlawn Drive, Honolulu, HI 96822, USA*
[3] *Hubble Fellow*

ABSTRACT

Some physical processes that occur during a star's main-sequence evolution also affect its post main-sequence evolution. It is well known that stars with masses above approximately 1.1 $M_\odot$ have well-mixed convective cores on the main sequence, however, the structure of the star in the neighborhood of the convective core regions is currently underconstrained. We use asteroseismology to study the properties of the stellar core, in particular, convective boundary mixing through convective overshoot, in such intermediate mass stars. These core regions are poorly constrained by the acoustic (p) mode oscillations observed for cool main sequence stars. Consequently, we seek fossil signatures of main sequence core properties during the subgiant phase of evolution. During the subgiant phase, modes of mixed character that sample the deep interior, can be observed. These modes sample the regions of the stars that are affected by the main-sequence structure of these regions. We model the global and near-core properties of 62 subgiants observed by the *Kepler*, K2, and TESS space missions. We find that the effective overshoot parameter, $\alpha_{\mathrm{ov,\,eff}}$, increases from $M = 1.0 M_\odot$ to $M = 1.2 M_\odot$ before flattening out. We situate these results within existing studies of main-sequence convective core boundaries.

Keywords: asteroseismology - stars: solar-type - stars: oscillations - stars: interiors

1. INTRODUCTION

Physical processes occurring within a star during its main-sequence dictate its future evolutionary history. Stars with masses above about 1.1 $M_\odot$ host well-mixed convective cores, but the structure of the regions near the outside of the convective core is currently not well understood. Physical processes such as convective overshooting, the process by which parcels of convective fluid pass the classical convective boundary because of their momentum, are thought to extend the well-mixed convective cores past the classical boundary, usually defined by the Schwartzchild or Ledoux criterion. Determining how best to model overshooting in 1-D stellar evolutionary codes is important, since incorporating core overshoot into stellar models increases the amount of hydrogen available to a main-sequence star, thereby increasing its main-sequence lifetime and altering the star's evolution, see Fig. 1. A better understanding of this convective boundary mixing will better anchor our calibration of absolute ages in stellar modelling, in turn clarifying the ages of other astrophysical systems of interest, such as Milky Way progenitors (Chaplin et al. 2020) and exoplanet hosts (Huber et al. 2019).

Convective overshoot from the stellar core is known to be necessary in order for stellar models to reproduce observations of eclipsing binaries (e.g. Schroder et al. 1997; Pols et al. 1997; Ribas et al. 2000; Claret 2007; Claret & Torres 2018, 2019; Claret et al. 2021; Constantino & Baraffe 2018; Costa et al. 2019) and the color-magnitude diagrams of clusters (e.g. Maeder & Mermilliod 1981; Aparicio et al. 1990; Bertelli et al. 1992; VandenBerg et al. 2006; Rosenfield et al. 2017). Extra mixing beyond the convective core is also known to emerge from numerical hydrodynamics, although internal gravity waves also contribute to the convective boundary mixing (e.g. Higl et al. 2021). See Anders & Pedersen (2023) for a recent review of observational and theoretical constraints on mixing processes at the convective boundaries in main-sequence stars.

Different investigations find that the amounts of core overshoot needed to match a star's observable quantities depend on global stellar properties. For example, Claret & Torres (2016) studied a sample of eclipsing binary stars with observed masses, radii, temperatures, and elemental abundances and found that the size of the overshoot region has a positive dependence on the stellar mass. This result remains debated due to uncertainties in calibrating convective overshoot using eclipsing binaries (Constantino & Baraffe

Corresponding author: Christopher Lindsay
christopher.lindsay@yale.edu

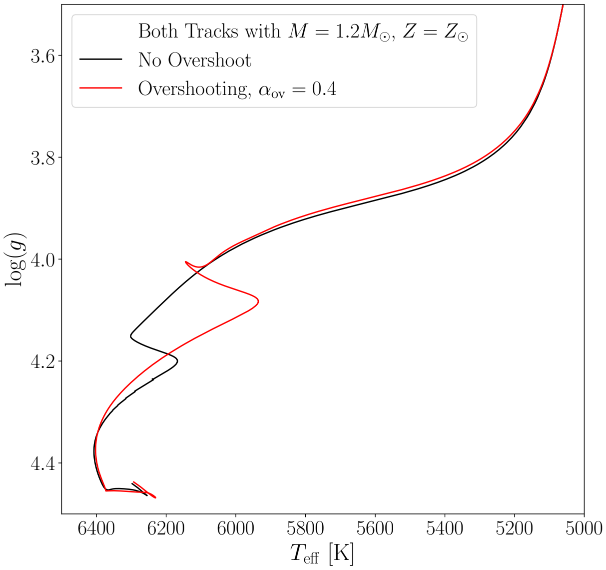

Figure 1. Two evolutionary tracks showing the effects of incorporating core overshooting into a stellar model. Both tracks show $M = 1.2M_\odot$, $Z = Z_\odot$ models evolved using MESA version r12778 from the pre-main sequence to the red giant branch. The track with overshooting parameter $\alpha_{\rm ov} = 0.4$, shown in red, shows that incorporating overshoot changes the evolution leading up the subgiant branch.

2018; Claret & Torres 2019) and the exact relationship between overshoot and stellar properties such as mass, metallicity, and evolutionary state remains uncertain. Even so, published grids of stellar evolution models also frequently make use of core overshooting prescriptions, typically scaling the amount of overshooting with stellar mass (Demarque et al. 2004; Pietrinferni et al. 2004; Bressan et al. 2012).

Asteroseismology, or the study of stellar oscillations, has provided the means to directly study the interiors of stars. The global oscillation properties of solar-like oscillations are $\nu_{\rm max}$, the frequency of maximum oscillation power, and $\Delta\nu$, the large frequency separation, have been used extensively to determine global stellar parameters (Yu et al. 2018), they cannot be used to probe the deep stellar interiors we are interested in. Additionally, even modelling individual p-mode (pressure-mode) oscillation frequencies cannot give us detailed insights into the near-core structure of main-sequence stars with convective cores. In a previous paper (Lindsay et al. 2023), we have shown that pure p-modes are not able to sample the near-core regions directly, making inferences about the amount of core overshooting occurring in main-sequence stars difficult for some targets. Instead of analyzing the global asteroseismic properties ($\nu_{\rm max}$ or $\Delta\nu$) or the p-mode oscillations of main-sequence stars, we study dipolar oscillation modes which exhibit mixed character, which only arise after a star leave the main sequence.

After a star depletes its reserves of hydrogen in the core, its core begins to contract while its envelope begins to expand. At this stage of evolution, hydrogen is burned in a thin shell surrounding the now inert helium core. Since the convective motions in the core have also ceased by the time the star becomes a subgiant, the chemical composition gradient in these overshooting regions, having been frozen in at the main-sequence turnoff, serve as a fossil signature of the main sequence structure around the convective core. At the same time, the contraction of the stellar core is accompanied by an expansion of the envelope outside the hydrogen burning shell, leading to a large density contrast between the stellar core and envelope, allowing the study of these inner layers through mixed-mode asteroseismology (see Hekker & Christensen-Dalsgaard 2017, for a review of evolved star asteroseismology). Thus, studying the structure of subgiant stars can answer questions about main-sequence processes occurring above convective cores, since the main-sequence structural details of the star will be frozen into the subgiant's inert core and the subgiant's structure render their inspection observationally feasible through the asteroseismic analysis of mixed modes.

The effects of main-sequence core overshoot on the structural properties of subgiants can be seen in Fig. 2. The left panel of the Fig. 2 shows the propagation diagrams of two main-sequence stellar models with the same mass and chemical compositions but with different amounts of convective core overshoot. While significant difference can be seen in the deep, near-core layers, these are inaccessible to inspection using non-radial p-modes. After a main-sequence star evolves to a subgiant (right panel of Fig. 2), a large density contrast develops between the stellar core and envelope. During this stage of evolution, $\ell = 1$ oscillation modes with frequencies near $\nu_{\rm max}$ may propagate in two different regions: the envelope, which supports pressure modes (p-modes where the restoring force is pressure, with frequencies $\nu \geq N$ and $S_{\ell=1}$ in both panels of Fig. 2) and the core, which supports gravity modes (g-modes where the restoring force is buoyancy, with frequencies $\nu \leq N$ and $S_{\ell=1}$ in the Fig. 2 propagation diagrams). The observed mixed modes couple these two regions, with g-like character in the core and p-like character in the envelope (Scuflaire 1974; Aizenman et al. 1977). We use individual mixed-mode oscillations, whose frequencies directly probe the core/envelope boundary, to investigate the properties and structures around stellar cores in this work.

Space based photometry missions such as CoRoT (Baglin et al. 2006), *Kepler* (Borucki et al. 2010), and *TESS* (Ricker et al. 2015) which observe many stars over long temporal baselines have made possible the observational detection of mixed modes in many stars possible. Since these mixed modes sample the interior layers of evolved stars near the core-envelope boundary, they can, and have been, used to constrain the amplitude of overshooting above convective cores. In particular, Deheuvels & Michel (2011) found from the CoRoT data of the solar-like oscillator HD49385 that the oscillation spectrum of the star can only be properly explained by an avoided crossing (a characteristic feature of on-resonance mixed modes), whose shape constrains the amount of core overshooting above the stellar core to either

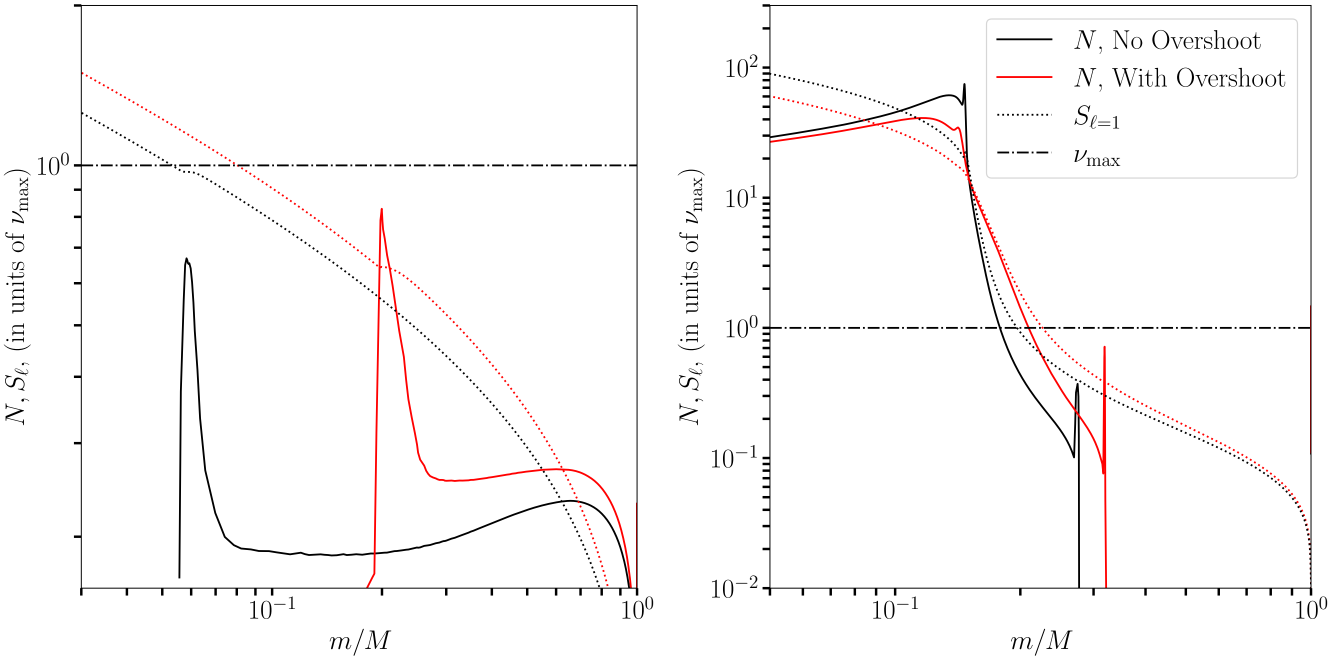

Figure 2. Propagation diagrams showing two $1.3M_\odot$ main sequence star stellar models (left panel) with and without overshooting. Both models' future subgiant structures are show in the right panel. The Brunt–Väisälä (buoyancy) frequency (N) is indicated with the solid lines, while the $\ell = 1$ Lamb frequency ($S_{\ell=1}$) is indicated with the dotted lines. The horizontal dot-dashed lines show the frequency of maximum oscillation power, $\nu_{\rm max}$. The models incorporating convective core overshoot with overshoot parameter $\alpha_{\rm ov} = 0.3$ are shown in red, while the models without overshoot are shown in black. Both models have the same initial metallicity ($[{\rm Fe/H}]_0 = -0.025$), initial helium abundance ($Y_0 = 0.284$), and mixing length parameter $\alpha_{\rm MLT} = 1.75$.

very small or moderate values. Deheuvels et al. (2016) also made seismic estimates of the extent of convective cores in 8 low mass main sequence stars using data from *Kepler*. Noll et al. (2021) then studied the Kepler subgiant, KIC10273246, and found again that accounting for core overshooting improved their models' agreement with the observed oscillation mode frequencies. Building on these studies, we now make similar measurements from an analysis using a grid based modelling approach to determine the interior properties of a larger sample of subgiants observed by *Kepler*.

In this paper, we look at a sample of 62 subgiants to determined how much convective core overshoot was present in these stars during their main sequence. Our objective in doing so is to determine relationships between global stellar properties and near core-mixing processes. For example, Viani & Basu (2020) examined 9 intermediate mass main-sequence stars from the *Kepler* LEGACY sample (Lund et al. 2017; Silva Aguirre et al. 2017) and found through asteroseismic modelling that the amplitude of convective overshoot from the main-sequence core increases with stellar mass. The rest of this paper is organized as follows. We discuss our sample of subgiant stars in section 2 and describe our grid of models in section 3. In section 4 we explain how we compare the observed spectroscopic and asteroseismic properties of the subgiant target stars to our model grid. In section 5 we show how the main-sequence core properties of the stars in our sample depend on the global stellar parameters and place our results into the context of other studies focused on determining the relationship between core overshoot properties and stellar parameters.

2. THE SAMPLE OF SUBGIANTS

We study a total of 62 subgiant stars in this work, 36 observed during the *Kepler* mission, 8 observed during the K2 mission, and 18 observed with TESS, of which 12 were observed in the TESS Southern Continuous Viewing Zone (CVZ) during its first year of operations. Fig. 3 shows a Kiel diagram (log(g) vs. Effective Temperature) of our sample of subgiant stars. The different missions observed the stars for varying lengths of time, consequently, the quality of the power spectra used to determine the oscillation frequencies varies tremendously.

2.1. *Kepler Subgiants*

The nominal *Kepler* mission ran for just over 4 years, giving the best possible scenario for determining the asteroseismic mode frequencies we require for our fitting procedure. For this work, like in Ong et al. (2021a), we study a sample of subgiants observed with short cadence which was already examined using a grid-based modeling approach (Li et al. 2020a,b). The mode frequencies used in our analysis were measured in Li et al. (2020b). The global asteroseismic parameters, $\Delta\nu$ and $\nu_{\rm max}$, for these targets were derived in Serenelli et al. (2017), while the spectroscopic observables $T_{\rm eff}$ and [Fe/H] were taken from Table 1 of Li et al. (2020a). When available, we also used stellar luminosity (L)

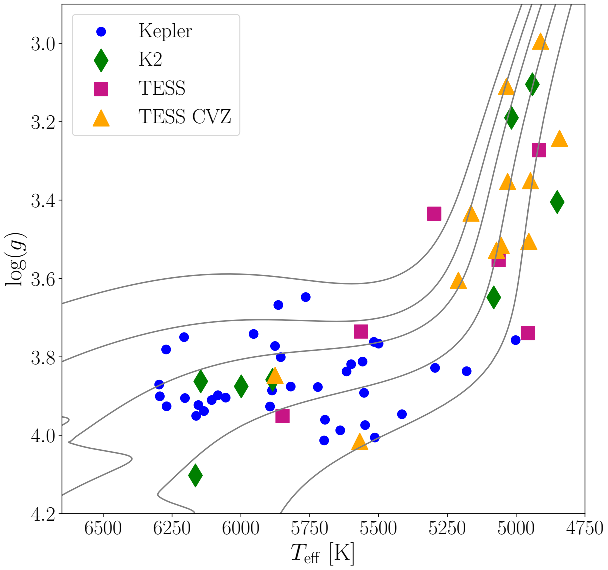

Figure 3. The sample of subgiant stars used in the work on a Kiel ($\log(g)$ vs. $T_{\rm eff}$) diagram. The different symbols refer to which mission observed the subgiant. The background gray curves show solar-abundance evolutionary tracks with masses between 1.0 and 1.8 $M_\odot$ in steps of $0.2M_\odot$. The tracks are for modes without core overshoot.

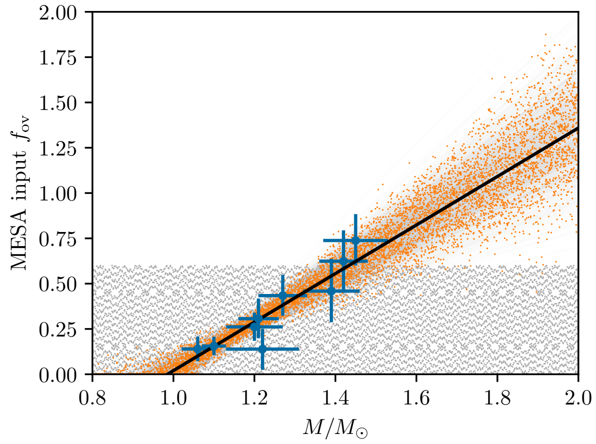

Figure 4. Comparison of sampling of the mass-overshoot plane in the model grid used in this work (gray points — Sobol sampling in a finite range) against that of the grid used in Ong et al. (2021a) (orange points — random sampling over the mass-overshoot relation of Viani & Basu 2020, shown with the blue points).

measurements derived from the Gaia mission Gaia Collaboration et al. (2018).

2.2. *K2 Subgiants*

The time series photometry available from the K2 mission are only about 75 days long in each campaign (Howell et al. 2014), with 60 second sampling at short cadence. This results in significantly degraded frequency resolution, and, since the photometric noise was also higher due to decreased pointing stability, only 8 K2 subgiants studied in Ong et al. (2021a) showed significant oscillation power excess. The oscillation frequencies and spectroscopic properties for these stars are the same as those used in Ong et al. (2021a) (see section 3.3), although the mode frequencies for some of these stars were reanalyzed in González-Cuesta et al. (2023).

2.3. *TESS Subgiants*

During its nominal mission, stars observed by TESS can, in the worst case, be observed for only a single sector (27 days) which is not much longer than the average oscillation mode lifetime. Therefore, in the frequency domain, the limited spectral resolution of the power spectrum is comparable to the mode line widths. In addition, the TESS pixels are much larger than Kepler's meaning the subgiant star oscillation mode frequencies derived from TESS photometry are more sensitive to noise and suffer from more contamination when compared with *Kepler*-derived subgiant mode frequencies. Since the detection and extraction of oscillation mode frequencies is not the focus of this work, our TESS sample of subgiants is relatively small and made from studies already communicated through the asteroseismology community. The spectroscopic and asteroseismic observables of our sample of 6 stars observed by the nominal TESS mission (β Hyi, δ Eri, η Cep, ν Ind, TOI 197, and HD 38529) is further described in section 3.2 of Ong et al. (2021a).

In addition to these 6 subgiants, our sample includes 12 subgiant stars observed by TESS in its Southern Continuous Viewing Zone. The oscillation mode frequencies for these stars were fitted against the power spectra using 7 different peakbagging pipelines (J. M. J. Ong, in preparation). The spectroscopic properties ($T_{\rm eff}$ and [Fe/H]) were taken from the 17th data release of the Sloan Digital Sky Survey (Abdurro'uf et al. 2022), while luminosity measurements were found with SED measurements in conjunction with GAIA parallaxes.

3. OUR GRID OF MODELS

There are two main classes of techniques to model the interiors of subgiant stars using asteroseismic and spectroscopic data. One that uses large scale grid searches to study many targets (as in McKeever et al. 2019; Jørgensen et al. 2020; Li et al. 2020a; Nsamba et al. 2021; Ong et al. 2021b,a), and another, where the parameter space of the grid is adapted to each target individually (as in Ball et al. 2018, 2020; Huber et al. 2019; Chaplin et al. 2020; Noll et al. 2021). These two approaches are often combined, with the results of coarser grid searches used to restrict the parameter space for further individual study. While boutique modelling involving optimization based parameter searches or individual dense grids created separately for each target is a good method for determining the properties of individual stars, it can be very slow and computationally expensive. Instead, we used a large scale grid search method for this study.

The grid we use in our fitting procedure is largely based on that used in Ong et al. (2021a). It consists of subgiant models created with MESA version r12778 (Paxton et al. 2011, 2013, 2015, 2018, 2019). These models use the solar chemical abundance mixture detailed in Grevesse & Sauval (1998), an Eddington gray atmospheric boundary condition, and the mixing-length prescription of Cox & Giuli (1968). Element diffusion was handled using the formulation of Thoul et al. (1994), and we included a mass-dependent scaling prefactor (see Viani et al. 2018). The parameters of the models in the grid, Sobol-sampled in almost an identical fashion to that used in Ong et al. (2021a), were the initial stellar mass ($M \in [0.8M_\odot, 2.0M_\odot)$, the mixing length parameter ($\alpha_{\rm mlt} \in [1.3, 2.2]$), initial metallicity ($[{\rm Fe/H}]_0 \in [-1, 0.5]$), and initial helium abundance ($Y_0 \in [0.176, 0.32]$). We construct models with sub-primordial ($Y_{\rm primordial} \sim 0.248$) to avoid edge-effects from our grid's construction affecting the fitting results, but we down-weight the likelihoods of stellar models with, $Y_0 < Y_{\rm primordial}$, as we explain in section 4. Convective overshoot from the stellar core was incorporated according to MESA's implementation of overmixing with a step profile (cf. §2 of Lindsay et al. 2022). Unlike the grid used in Ong et al. (2021a), we Sobol-sample the step overmixing parameter, $\alpha_{\rm ov}$, between 0 and 0.6, as shown in Fig. 4.

The result of MESA's implementation of step overmixing is that the well-mixed stellar core extends beyond the Schwarzschild boundary by a distance $r_{\rm ov}$, given by

$$r_{\rm ov} = \begin{cases} \alpha_{\rm ov} H_p & \text{if } H_p \le r_{\rm cz} \\ \alpha_{\rm ov} r_{\rm cz} & \text{if } H_p > r_{\rm cz} \end{cases}, \tag{1}$$

where H_p is the pressure scale height at the convective boundary and $r_{\rm cz}$ is the radius of the core convection zone. This ensures that when the convective core is very small, the overshooting region does not become unphysically large, as would be the case for overshooting by $\alpha_{\rm ov} H_p$. Another feature of the MESA implementation of step overmixing is that the overshoot region does not start exactly at the Schwarzschild boundary (estimated by where $\nabla_{\rm radiative} = \nabla_{\rm adiabatic}$) but rather begins at a location $f_0 H_p$ into the convective core from the Schwarzschild boundary. This is because the mixing coefficient approaches 0 at the Schwarzschild boundary. In our grid, f_0 is set to 0.005. In order to avoid confusion when referencing the step overshooting parameter, and to make it easier to compare our results with studies that used other stellar evolutionary codes, we save the following three different overshoot parameters in our grid.

1. Input Overshoot, $\alpha_{\rm ov}$: This is the value entered into the MESA controls inlist when creating the stellar model tracks. We varied this parameter in our grid from 0 to 0.6.

2. Scaled Overshoot, $\alpha_{\rm ov,\,scaled}$: We define Scaled Overshoot based on the input overshoot parameter as $\alpha_{\rm ov,\,scaled} = \alpha_{\rm ov} \min(r_{\rm cz}/H_p, 1) - f_0$ where $\alpha_{\rm ov}$ is the input overshoot parameter, $r_{\rm cz}$ is the radius of the MESA-defined convective zone, H_p is the pressure scale height at the convective zone boundary, and f_0 is equal to 0.005.

3. Effective Overshoot, $\alpha_{\rm ov,\,eff}$: The effective overshoot parameter is calculated directly from the MESA-generated profile file for the time step at which the MESA-defined convective core mass was at its maximum. We define the effective overshoot parameter as $\alpha_{\rm ov,\,eff} = (r_{\rm well\text{-}mixed} - r_{\rm cz})/H_p$ where $r_{\rm well\text{-}mixed}$ is the well-mixed core boundary, defined by looking for the central-most grid point where the gradient of the mean molecular weight gradient, $\frac{\partial \nabla_\mu}{\partial r}$, spikes to at least $|\frac{\partial \nabla_\mu}{\partial r}| = 0.001 {\rm cm}^{-1}$.

For the subsequent analysis of the scaled and effective overshoot parameters, $\alpha_{\rm ov,\,scaled}$ and $\alpha_{\rm ov,\,eff}$ are both set to 0 in our grid if the corresponding model tracks maintain a convective core for less than 25% of their main sequence lifetime. This ensures that the overshoot parameters for models which do not maintain a convective core is 0.

The grid input parameters which we vary, M, $\alpha_{\rm mlt}$, $[{\rm Fe/H}]_0$, Y_0, and $\alpha_{\rm ov}$, are distributed uniformly using joint Sobol sequences of length 16382 over the ranges described previously. Each of these tracks were evolved using MESA from the pre-main sequence until the point where $\Delta\nu = 9\mu$Hz (following Ong et al. 2021a). For each subgiant model in our grid, the oscillation mode frequencies are calculated using GYRE version 6.0 (Townsend & Teitler 2013). The radial and quadrupole ($\ell = 0$ and $\ell = 2$) p-mode frequencies are calculated within $\pm 6\Delta\nu$ of $\nu_{\rm max}$. For the dipole ($\ell = 1$ modes, we calculated both π-mode and γ-mode frequencies and mixed-mode coupling matrices according to the mode isolation construction of Ong & Basu (2020). π-modes refer to the pure p-modes whose frequencies only depend on the p-mode cavity of the stellar model, while γ-modes refer to the pure g-modes whose frequencies only depend on the g-mode cavity; mixed modes are those linear combinations of π and γ modes that are also eigenfunctions of the wave operator. Following Ong et al. (2021a), we compute γ-mode frequencies and matrix elements for γ modes from a lower-bound frequency of $\nu_{\rm max} - 7\Delta\nu$ up to $n_g = 1$ γ-mode. The $\ell = 0$ and $\ell = 2$ modes, as well as the $\ell = 1$ $\pi-$ modes were corrected for inadequate modelling of the near surface layers (surface effects or surface term), before comparison with the observed mode frequencies, as discussed further in section 4.

4. MODELLING PROCEDURE

Many grid-based pipelines have been used to analyze asteroseismic data from spaced based missions, including those described in Basu et al. (2010); Gai et al. (2011); Campante et al. (2019); Stello et al. (2022), among others. Cunha et al. (2021) compared different asteroseismic pipelines using artificial asteroseismic data.

For this work, we start with a given set of observables and corresponding uncertainties for a target star. In this work, these include the spectroscopic parameters effective temperature ($T_{\rm eff}$), metallicity ([Fe/H]), and when available, Luminosity (L). These variables are used to define the spectroscopic likelihood. The global asteroseismic observables, $\Delta\nu$

and $\nu_{\rm max}$, are also used just in the down-selection of the large grid.

4.1. *Down-selecting the Complete Grid*

The first step in our modelling procedure is to search for all models in the complete grid with properties close to the target subgiant's observed values of $T_{\rm eff}$, [Fe/H], $\Delta\nu$, and $\nu_{\rm max}$. We calculate a penalty function based on individual χ^2 values for each observed parameter, P, given by,

$$\chi^2_P = \frac{(P_{\rm obs} - P_{\rm model})^2}{\sigma^2_{P_{\rm obs}}}, \tag{2}$$

and the total χ^2 is given by

$$\chi^2_{\rm downselect} = \chi^2_{T_{\rm eff}} + \chi^2_{\rm [Fe/H]} + \chi^2_{\Delta\nu} + \chi^2_{\nu_{\rm max}}. \tag{3}$$

If luminosity is available for the target star, we include χ^2_L in the calculation of$\chi_{\rm downselect}$. We down-select the complete grid to models satisfying $\chi^2_{\rm downselect} < 10^2$. This greatly reduces computational cost by restricting the number of models requiring an expensive seismic likelihood evaluation from more than 14 million (the whole grid) to around ten thousand models per target subgiant star.

4.2. *Spectroscopic Likelihoods*

To quantify how well the models in the down-selected grid matches the spectroscopic observables of the target subgiant, we calculate the following spectroscopic cost function,

$$\chi^2_{\rm spec} = \chi^2_{T_{\rm eff}} + \chi^2_{\rm [Fe/H]} + \chi^2_L \tag{4}$$

following Equation 2. For the 6 target stars for which we could not find reliable luminosity measurements, we omitted χ^2_L from the calculation of χ^2_{spec}. These stars are KIC6442183, KIC11137075, KIC11414712, EPIC212478598, EPIC246305274, and δ Eri.

The spectroscopic likelihood for every model in the down-selected grid is then calculated as

$$\mathcal{L}_{\rm spec} = \exp\left(-\frac{\chi^2_{\rm spec}}{2}\right). \tag{5}$$

Finally, we find the normalized spectroscopic likelihoods, $\mathcal{L}_{\rm spec,\,norm}$, by dividing each model's spectroscopic likelihood by the sum of all spectroscopic likelihoods in the down-selected grid, such that the sum of all the normalized spectroscopic likelihoods is 1.

4.3. *Seismic Likelihoods*

In order to calculate a seismic cost function, we must quantify how well a stellar model's oscillation mode frequencies match the observed frequencies of a given target. To do this, the model's set of oscillation modes must be compared to the set of observed modes, which entails matching each of the observed oscillation mode frequencies to a corresponding model mode frequency. The model modes also must be corrected for the surface effect, a frequency-dependent error in stellar model oscillation mode frequencies caused by our inability to model the near-surface layers of a star in one dimension.

We match the model oscillation mode frequencies to the observed frequencies in two different ways, depending on the angular degree (ℓ) of the mode. The radial and quadrupole modes ($\ell = 0$ and 2) are matched based on their inferred values of radial order n_p. We infer the n_p values of the observed modes based on the observed mode frequency, the observed $\Delta\nu$ as $n_{\rm p,\,obs} = (\nu_{\rm obs}/\Delta_\nu) - (\ell/2)$. The n_p values for a models' oscillation frequencies are returned from GYRE along with the mode frequencies. The matched $\ell = 0$ and 2 modes are then used to determine the coefficients of the two-term surface term from Ball & Gizon (2014) by minimizing the quantity,

$$\sum_{\ell\in\{0,2\}} \sum_{n_p=0}^{N} \frac{\nu_{{\rm obs,\,n}_p\ell} - (\nu_{{\rm model,\,n}_p\ell} + \delta\nu_{{\rm surf,\,n}_p\ell})}{\sigma_{\nu,{\rm obs,\,n}_p\ell}} \tag{6}$$

where n denotes the radial order of the mode, ℓ denotes the angular degree of the mode, N is the total number of modes, $\nu_{{\rm obs,\,n}\ell}$ is the observed mode frequency, $\sigma_{\nu,{\rm obs,\,n}\ell}$ is that modes associated frequency error, $\nu_{{\rm model,\,n}\ell}$ is the uncorrected model mode frequency, while $\delta\nu_{{\rm surf,\,n}\ell}$ is the two term parametric correction of Ball & Gizon (2014). This correction is given by,

$$\delta\nu_{{\rm surf,\,n}_p\ell} = \frac{1}{I_{{\rm n}_p\ell}}\left(a_{-1}\left[\frac{\nu_{{\rm n}_p\ell}}{\nu_0}\right]^{-1} + a_3\left(\frac{\nu_{{\rm n}_p\ell}}{\nu_0}\right)^3\right), \tag{7}$$

where $\nu_{{\rm n}\ell}$ is the model mode frequency, $I_{{\rm n}\ell}$ is the model mode inertia, ν_0 is set to $\nu_{\rm max}$, and the coefficients (a_{-1} and a_3) are chosen to minimize the quantity in Eq. (6).

The above procedure gives us surface corrected model mode frequencies for $\ell = 0$ and $\ell = 2$ modes, and we can now define $\nu_{\rm model,\,corr} = \nu_{\rm model,\,uncorr} + \delta\nu_{\rm surf}$. For the $\ell = 1$ modes though, following Ong et al. (2021c), we apply the surface correction to the dipole π modes, and recover surface-corrected model mixed modes by coupling these surface corrected π modes to the γ modes, which remain unaffected by surface effects (Ong & Basu 2020). Surface-corrected dipole ($\ell = 1$) mode frequencies are matched to the observed mode frequencies using an iterative nearest-neighbor search.

Next, for each combination of models in the down-selected grid and subgiant target, we calculate a seismic cost function with the form,

$$\chi^2_{\rm seis} = \mathcal{W}_\nu \frac{1}{N_\nu} \sum_{n}^{N_\nu} \left(\frac{\nu_{{\rm obs},n} - \nu_{{\rm model},n}}{\sqrt{\sigma^2_{\nu_{{\rm obs},n}} + \sigma^2_{\nu,{\rm eff}}}}\right)^2, \tag{8}$$

where N_ν refers to the total number of matched oscillation modes in the set, $\mathcal{W}_\nu$ is a weighting term that we describe later. $\sigma_{\nu,\,\rm eff}$ accounts for the systematic error in the modeling due to grid undersampling (following Li et al. 2020a; Ong et al. 2021a). We first calculate the seismic cost function

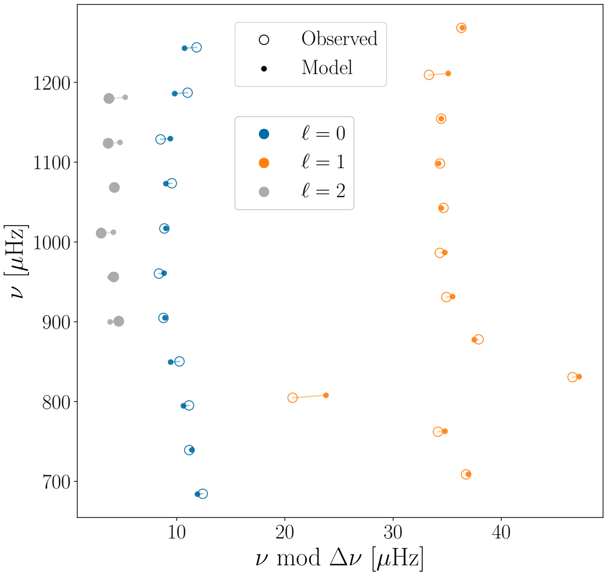

Figure 5. The best mode match for the subgiant target KIC4346201, as determined by minimizing Eq. (8) for all models in the down-selected grid (with $\sigma_{\nu,\,\mathrm{eff}}$ set to 0). The observed modes are shown with open circles, and the surface-corrected modes of the model are shown with dots. Each observed mode is connected to its corresponding model mode with a line. The colors of the points and lines indicate the angular degree of the modes ($\ell = 0$ in blue, $\ell = 1$ in orange, and $\ell = 2$ in gray.

(Eq. (8)) with $\sigma_{\nu,\,\mathrm{eff}}$ set to 0 to identify the best fit model. As an illustrative example, the best mode match for the subgiant target KIC4346201 is shown in Fig. 5. Then we set $\sigma_{\nu,\,\mathrm{eff}}$ as the root-mean-squared difference between the observed mode frequencies and the best fitting model's surface corrected mode frequencies.

The surface term makes the model mode frequencies larger than the observed frequencies, and this difference increases with frequency. The model of the surface term shown in Eq. (7) does not take this into account, and it is possible that after the surface term correction, a model that has frequencies lower than the observed frequencies would end up with a smaller χ^2_{seis} than a model with the expected behavior of the surface term. To account for this, we add a weight, $\mathcal{W}_\nu$, in Eq. (8) to give a larger weight to models whose uncorrected frequencies were larger than the observed frequencies. To do this, we assign $\mathcal{W}_\nu$ a value of 0.5 if all model mode frequencies are higher than their corresponding observed frequencies. If this condition is not satisfied, we set $\mathcal{W}_\nu$ to 1.

For models with interiors that match observed stars, it is a known property of the surface term that the frequency differences between the observed and model p-modes should be largest at high frequencies, and lowest at low frequencies. We follow Basu & Kinnane (2018) and Ong et al. (2021b) in accounting for this by adding another penalty function to χ^2_{seis} with the form,

$$\chi^2_{\mathrm{low}\ n} = \frac{1}{4}\frac{1}{10}\sum_{n}^{4}\left(\frac{\nu_{\mathrm{obs},n}-\nu_{\mathrm{model},n}}{\sqrt{\sigma^2_{\nu_{\mathrm{obs},n}}+\sigma^2_{\nu,\mathrm{eff}}}}\right)^2. \tag{9}$$

The factor 1/4 comes from the number of modes that we are summing, and the factor 1/10 gives a lower weight to $\chi^2_{\mathrm{low}\ n}$ compared to χ^2_{seis}, calculated in Eq. (8). We do this because this term is incorporated for the purpose of regularization, and is not meant to influence the overall posterior distribution.

For each of the 62 targets in our sample of subgiants, we calculate the two terms (χ^2_{seis} and $\chi^2_{\mathrm{low}\ n}$) of the seismic cost function. We then calculate a seismic likelihood ($\mathcal{L}_{\mathrm{seis}}$) for each model in the target star's associated down-selected grid as

$$\mathcal{L}_{\mathrm{seis}} = \exp\left[-\frac{\left(\chi^2_{\mathrm{seis}}+\chi^2_{\mathrm{low}\ n}\right)}{2}\right]. \tag{10}$$

The normalized seismic likelihood, $\mathcal{L}_{\mathrm{seis,\ norm}}$, is also calculated in the same way as for $\mathcal{L}_{\mathrm{spec,\ norm}}$ by dividing all the model's values of $\mathcal{L}_{\mathrm{seis}}$ by the sum of all $\mathcal{L}_{\mathrm{seis}}$ values in the down-selected model grid, such that $\sum \mathcal{L}_{\mathrm{seis,\ norm}} = 1$.

4.4. *Estimating Stellar Parameters*

For each of the stars in our sample, we determine total likelihoods, $\mathcal{L}_{\mathrm{tot}}$, for each model in the down-selected grid by combining the spectroscopic and seismic normalized likelihoods as

$$\mathcal{L}_{\mathrm{tot}} = t_{\mathrm{model}} \times \mathcal{W}_{\mathrm{He}} \times \mathcal{L}_{\mathrm{seis,\ norm}} \times \mathcal{L}_{\mathrm{spec,\ norm}} \tag{11}$$

where t_{model} is a time interval defined below, and $\mathcal{W}_{\mathrm{He}}$ is a helium weight. By using the normalized seismic and spectroscopic likelihoods, we ensure that neither component of the cost function dominates the overall total likelihood. t_{model} is the length of time (in seconds) each model spends during that model's specific MESA time step, and is included to down-weight the likelihoods of models in portions of the model grid which are more densely sampled in time. $\mathcal{W}_{\mathrm{He}}$ is given by

$$\mathcal{W}_{\mathrm{He}} = \begin{cases} 1 & \text{if } Y_0 > Y_{\mathrm{p}} \\ \exp\left[-\left(\frac{(Y_0 - Y_{\mathrm{p}})}{0.016}\right)^2\right] & \text{if } Y_0 \le Y_{\mathrm{p}} \end{cases}, \tag{12}$$

with $Y_{\mathrm{p}} = 0.248$ (Steigman 2010). The total likelihood of a given model incorporates this weight term in order to penalize models with initial helium abundance lower than the primordial value of helium, Y_p.The helium-weighted total likelihoods are also normalized, leaving us with an associated likelihood value, $\mathcal{L}_{\mathrm{tot,\ norm}}$ for every model in the target star's down-selected grid.

To obtain the best fit parameters and parameter errors for each of the subgiants in our sample (section 2), we calculate the likelihood weighted means of each parameter saved

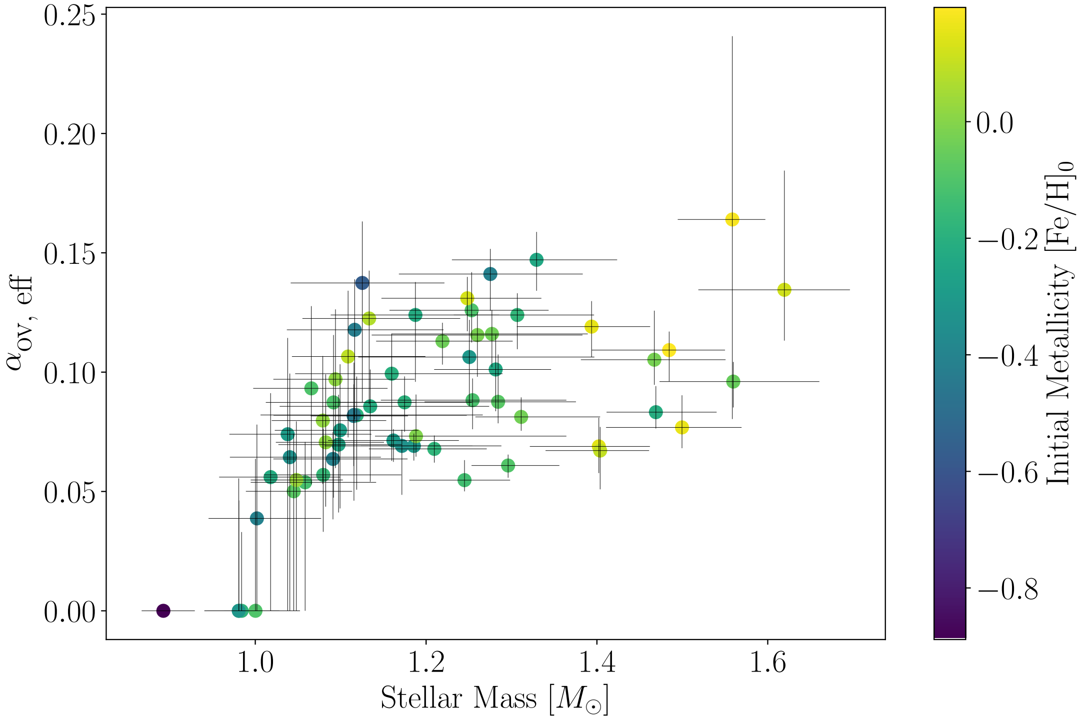

Figure 6. Effective overshoot parameter $\alpha_{\mathrm{ov,\ eff}}$ versus stellar mass for our sample of 62 subgiants. The points are colored by the modelling results for initial metallicity. Each point's position and color represents the 50th percentiles of the given parameter for each target. The error bars are given by the 16th and 84th percentiles of each parameter's posterior distribution.

in the grid discussed in section 3 10,000 times for different realizations of the spectroscopic parameters. The likelihood weighted mean for a given parameter, $\bar{P}$, is calculated as,

$$\bar{P} = \frac{\sum_{i=0}^{N}(\mathcal{L}_{\mathrm{tot,\ norm}_i} P_{\mathrm{model}_i})}{\sum_{i=0}^{N}(\mathcal{L}_{\mathrm{tot,\ norm}_i})}, \tag{13}$$

where N is the number of models in a subgiant target's downselected grid and P_{model} is the model parameter.

We draw 10,000 sample values of each parameter from a normal distribution with the mean equal to the literature-reported value of the parameter and standard deviation equal to the reported error, as was done in Ong et al. (2021a). Each sampling of the spectroscopic parameters results in a different likelihood weighted mean for our model output parameters, and hence, performing a Monte–Carlo over the spectroscopic parameters allows us to determine posterior distributions of our output parameters. The 16th, 50th, and 84th percentiles of the posterior distributions for stellar mass (M), radius (R), luminosity (L), temperature (T_{eff}), age, initial metallicity ($[\mathrm{FeH}]_0$), initial helium abundance (Y_0), mixing length (α_{mlt}), and effective overshoot parameter ($\alpha_{\mathrm{ov,\ eff}}$) are listed in tables Table 1 and Table 2 for the stars observed by *Kepler* and TESS respectively.

5. RESULTS AND DISCUSSION

Fig. 6 shows the results for the effective overshoot parameter ($\alpha_{\mathrm{ov,\ eff}}$) as a function of the stellar mass. The errors bars for both parameters show the 16th and 84th percentiles of the output parameter posterior distributions. We can see that for sufficiently low mass stars ($M \leq 1.0 M_\odot$) the modelled $\alpha_{\mathrm{ov,\ eff}}$ is 0. This is because the stellar models at this mass do not maintain a convective core for a sufficiently long amount of time (> 25% of their main sequence lifetimes.) At slightly higher masses, from $M \approx 1.0 M_\odot$ to $M \approx 1.15 M_\odot$, the value of the effective overshoot parameter increases with stellar mass from $\alpha_{\mathrm{ov,\ eff}} \lesssim 0.05$ to $\alpha_{\mathrm{ov,\ eff}} \approx 0.1 - 0.15$. At masses higher than $1.2 M_\odot$, our results for $\alpha_{\mathrm{ov,\ eff}}$ are seemingly independent of stellar mass. The points in Fig. 6 are colored by our initial metallicity ($[\mathrm{Fe/H}]_0$) results. We do not see a strong relationship between our results for $\alpha_{\mathrm{ov,\ eff}}$ and $[\mathrm{Fe/H}]_0$.

To place our results shown in Fig. 6 into context, we compare them with other studies of convective core overshooting. Studies that have used asteroseismic data to estimate overshooting in main-sequence convective cores have been carried out by Deheuvels et al. (2016), Viani & Basu (2020), and Noll & Deheuvels (2023), directly measuring the extent of the well-mixed convective core in a total of 19 main sequence stars (9 by Viani & Basu (2020), 8 by Deheuvels et al. (2016), and 2 by Noll & Deheuvels (2023)). In addition, Noll et al. (2021) modelled one subgiant star and produced an estimate for that star's convective core overshooting parameter. Fig. 7 shows our $\alpha_{\mathrm{ov,\ eff}}$ vs stellar mass results alongside the results of Deheuvels et al. (2016), Viani & Basu (2020), Noll et al. (2021), and Noll & Deheuvels (2023).

Overall, the results from this work agrees with the previous overshooting versus mass results from Deheuvels et al. (2016), Noll et al. (2021), and Noll & Deheuvels (2023), as

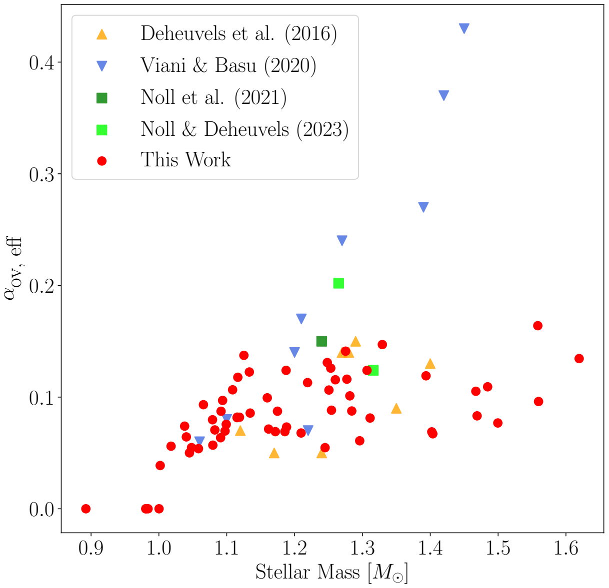

Figure 7. $\alpha_{\mathrm{ov,\,eff}}$ versus stellar mass results (red points) in comparison with other asteroseismic studies of convective core overshoot.

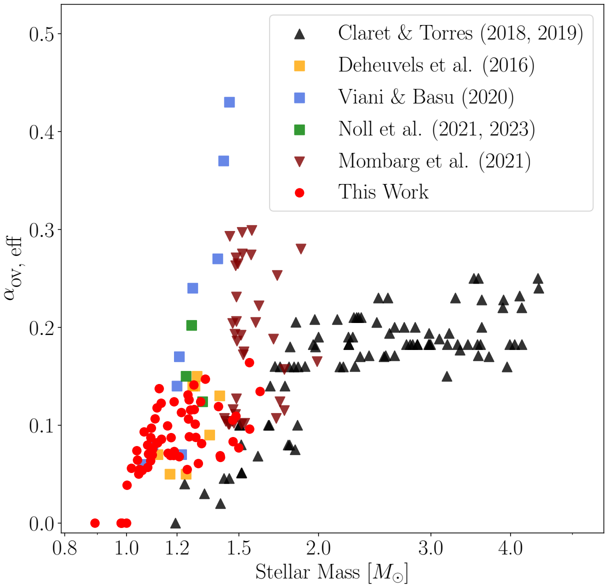

Figure 8. Our $\alpha_{\mathrm{ov,\,eff}}$ versus stellar mass results (red points) in comparison with other studies of convective core overshoot, including those shown in Fig. 7 as well as the eclipsing binary work of Claret & Torres (2018) and Claret & Torres (2019), shown in black triangles. The machine learning results for γ Doradus stars from Mombarg et al. (2021) are shown in maroon triangles.

well as with the results at the low mass end of the sample from Viani & Basu (2020). The spread in our reported values of $\alpha_{\mathrm{ov,\,eff}}$ for stars in the mass range of $1.1M_{\odot} \leq M \leq 1.4$ is also similar to the spread in the overshoot amplitude results of Deheuvels et al. (2016), for the same range of masses.

On the higher mass end of their sample ($M \geq 1.3M_{\odot}$), Viani & Basu (2020) reported significantly larger values of effective overshoot parameter, when compared with our results for stars in our sample with comparable masses. We identify two possible reasons for this discrepancy. First, the models calculated in Viani & Basu (2020) had set the temperature gradient, ∇ to ∇_{ad} in the convective overshooting regions above the models' convective cores. This is analogous to the "Step Penetrative Overshoot" we describe in section 2 of Lindsay et al. (2022) or the "convective penetration" described in Anders & Pedersen (2023). As shown in figure 8 of Viani & Basu (2020), the effective overshoot parameter results are larger, for a given stellar mass, if the stellar models used in the analysis maintained an adiabatic temperature gradient in the overshooting region. This temperature gradient difference alone cannot fully explain the large discrepancy between our results and the results of Viani & Basu (2020). The second major difference between the two modelling methods is that our modelling procedure sampled $\alpha_{\mathrm{ov,\,input}}$ far more densely (see Fig. 4) when compared to the procedure of Viani & Basu (2020), which only allowed about 8 different $\alpha_{\mathrm{ov,\,input}}$ values per target star. The denser sampling of both $\alpha_{\mathrm{ov,\,input}}$ and initial mass in our work results in more precise results of stellar mass and overshoot parameter, whereas the sparse sampling of $\alpha_{\mathrm{ov,\,input}}$ in Viani & Basu (2020). means that one model with a high overshooting parameter could dominate the likelihood function and significantly increase the output $\alpha_{\mathrm{ov,\,eff}}$ result. It should also be noted that the Viani & Basu (2020) models did not include the gravitational settling of heavy elements, and this too could increase their estimate of overshoot, however, that is unlikely to explain the large difference.

Mombarg et al. (2019) and Mombarg et al. (2021) studied convective core overshoot properties in intermediate mass stars through asteroseismology of γ Doradus stars. Mombarg et al. (2021) used machine learning techniques to study core overshooting in the same sample of stars from Mombarg et al. (2019), and we show how our results compare to theirs in Fig. 8. We note that the masses of the stars in their sample are higher than most of the stars in our sample. The reported exponential overshoot parameters, f_{ov} from Mombarg et al. (2021) are multiplied by 10 before plotting in Fig. 8, as Mombarg et al. (2021) uses the conversion factor of 10 in their analysis. We also include the stellar mass and overshooting amplitude results of Claret & Torres (2018) and Claret & Torres (2019) in Fig. 8. The stars studied in these works were higher-mass main-sequence stars in double line eclipsing binary systems, with $M \geq 1.2M_{\odot}$. Claret & Torres (2018) and Claret & Torres (2019) modelled the stars' masses and core overshoot parameters by comparing the observed masses, radii, and effective temperatures of the stars to stellar models made with varying amounts of convective core overshoot. In order to convert the exponential overshoot parameters, f_{ov}, reported in Claret & Torres (2019) to step overshooting parameters, α_{ov}, we follow Claret & Torres (2019) and multiply the reported values of f_{ov} by 11.36 ($11.36f_{\mathrm{ov}} = \alpha_{\mathrm{ov}}$) before plotting those points in Fig. 8. When a star is reported in both Claret & Torres (2018) and Claret & Torres (2019), we plot the value from Claret & Torres (2019).

Comparing our results (red points in Fig. 8) to the results of Claret & Torres (2018), Claret & Torres (2019), and Mombarg et al. (2021) shows significant differences in stellar mass/overshooting amplitude relationship. The combined results of Claret & Torres (2018) and Claret & Torres (2019) show the overshoot amplitude increasing with stellar mass from $\alpha_{\rm ov,\, eff} \approx 0$ at $M = 1.2 M_\odot$ to $\alpha_{\rm ov,\, eff} \gtrsim 0.15$ at $M = 2.0 M_\odot$. On the other hand, for the same mass range, Mombarg et al. (2021) finds that the step overshooting parameters for their sample of γ Doradus stars are larger in magnitude ($\alpha_{\rm ov,\, eff} > 0.1$) and less dependent on stellar mass.

Although our sample of subgiant stars do not go past masses of $M \approx 1.5 M_\odot$, we report higher values of $\alpha_{\rm ov,\, eff}$ for stars in the mass range of 1.2 to 1.5 $M_\odot$ range when compared to the eclipsing binary work of Claret & Torres (2018), Claret & Torres (2019). The majority of the γ Doradus stars studied by Mombarg et al. (2021) appear to have higher values of $\alpha_{\rm ov,\, eff}$ compared to the results from our sample of subgiants at similar masses. This is not an apples to apples comparison though, since we are using detailed asteroseismic data of individual oscillation modes while Claret & Torres (2018) and Claret & Torres (2019) produced their overshooting results based on the masses, radii, and effective temperatures of binary stars, without asteroseismology, while Mombarg et al. (2021) trained a machine learning model to return stellar masses and overshoot parameters based on observed period spacings between adjacent modes. In addition, the grid of models used in this work sampled the input parameters more densely, and covered a wider range of parameters when compared to the grids of models used in the eclipsing binary and γ Doradus work. Finally, the models calculated by Claret & Torres (2018), Claret & Torres (2019), and Mombarg et al. (2021) implemented penetrative overshoot which, as discussed previously, would cause higher output values of $\alpha_{\rm ov,\, eff}$, when compared with an analysis done with models with a radiative temperature gradient in the overshooting region.

Overall, Fig. 7 and Fig. 8 show that our stellar mass versus overshooting results agree well with other studies in the literature which use asteroseismology to study main-sequence stars (Deheuvels et al. 2016; Noll & Deheuvels 2023) though differ from asteroseismic results at the high mass end of our subgiant sample (Viani & Basu 2020; Mombarg et al. 2021). The differences between the overshooting results at high stellar mass could be a result of how the stellar models were constructed (a radiative versus an adiabatic temperature gradient in the overshooting region), but could also dependent on how dense the model grids in each study sampled the input parameters (M, Y_0, $[\rm Fe/H]_0$, $\alpha_{\rm mlt}$, and $\alpha_{\rm ov,\, input}$), in addition to what input data are used (individual mode frequencies are used in this work, while other works used global stellar parameters).

6. SUMMARY AND CONCLUSION

We have conducted a study analyzing 62 subgiant stars with high quality asteroseismic data from *Kepler* and TESS. The goal of this work was to better understand convective overshooting above main sequence star convective cores, a process by which moving parcels of fluid in the well-mixed convective core overshoot the classical convective boundary, leading to extra mixing above the core and a prolonged main sequence lifetime. Previous studies have analyzed main sequence convective core properties using asteroseismology, but the total number of targets that are bright enough and in the mass range of interest is quite small (Deheuvels et al. 2016; Noll & Deheuvels 2023). Additionally, Lindsay et al. (2023) showed that core regions of stars are poorly constrained by non-radial p-mode oscillations on the main sequence. Therefore, we analyze subgiant stars, which are much brighter, and whose dipolar mixed-mode oscillation frequencies sample the interior structures of subgiants. The main sequence structure of stars with convective cores (occurring when $M_\star \gtrsim 1.1 M_\odot$) alter the stellar structure, and these effects persist after the main sequence, when the star evolves into a subgiant (see Fig. 2).

Our sample of 62 subgiant stars consisted of 45 stars observed during the *Kepler* and K2 missions, as well as 17 stars observed with TESS. The spectroscopic parameters, as well the individual oscillation mode frequencies, were taken from various different literature sources (see section 2). To determine the amount of convective core overshooting, as well as the other properties of the stars in our sample, we implement a grid-based modelling technique, as opposed to performing a boutique modelling of every star in our sample. The grid we use densely samples stellar mass, mixing length, initial helium abundance, metallicity, and the input overshoot parameter, $\alpha_{\rm ov,\, input}$. The model tracks were calculated using MESA (Paxton et al. 2011, 2013, 2015, 2018, 2019; Jermyn et al. 2023) and the model oscillation mode frequencies were calculated using GYRE (Townsend & Teitler 2013). We match the observed mode frequencies of each star in our sample to the surface corrected model mode frequencies for each model in a down selected grid, based on the observed global properties of the target star. Using the matched mode frequencies, we then calculate a seismic cost function (Eq. (8)), as well as the associated seismic likelihood (Eq. (10)) for each combination of star and model. These seismic likelihoods are combined with a spectroscopic likelihood (Eq. (5)) to produce a combined 'total' likelihood (Eq. (11)), which we use to determine the likelihood weighted mean parameter values for all the different quantities in our model grid. The posterior distributions of our output quantities were determined by taking 10,000 samples of the spectroscopic observables and recalculating the likelihood weighted mean parameter values for each random sample.

These modelling results of the stars observed by *Kepler* are detailed in Table 1 while Table 2 contains our results for the stars observed by TESS. Our results for stellar mass and effective overshoot parameter, $\alpha_{\rm ov,\, eff}$, are visualized in Fig. 6 which shows that $\alpha_{\rm ov,\, eff}$ increases with stellar mass from $M = 1.0 M_\odot$ to $M = 1.2 M_\odot$. For stars with masses greater than 1.2 $M_\odot$ our results indicate a weak, or no correlation between stellar mass and overshooting amplitude. We compare these findings to previous work in section 5 while discussing how differences between our results and previous works can be explained by differences in modelling procedure.

CJL would like to thank Y. Asali, D. Bowman, M. Michielsen, J. Mombarg, J. Guerra, I. Pasha, M. G. Pedersen, J. van Saders, and R. Townsend for insightful and helpful discussions. We thank the Yale Center for Research Computing for guidance and use of the research computing infrastructure. SB and CJL acknowledges support from NSF grant AST-2205026. CJL also acknowledges support of a Gruber Science Fellowship. JMJO acknowledges support from NASA through the NASA Hubble Fellowship grants HST-HF2-51517.001-A, awarded by STScI, which is operated by the Association of Universities for Research in Astronomy, Incorporated, under NASA contract NAS5-26555.

Software: MESA (Paxton et al. 2011, 2013, 2015, 2018, 2019; Jermyn et al. 2023), GYRE (Townsend & Teitler 2013) , SciPy (Virtanen et al. 2020), Pandas (Reback et al. 2021)

REFERENCES

Abdurro'uf, Accetta, K., Aerts, C., et al. 2022, ApJS, 259, 35

Aizenman, M., Smeyers, P., & Weigert, A. 1977, A&A, 58, 41

Anders, E. H., & Pedersen, M. G. 2023, Galaxies, 11, 56

Aparicio, A., Bertelli, G., Chiosi, C., & Garcia-Pelayo, J. M. 1990, A&A, 240, 262

Baglin, A., Auvergne, M., Barge, P., et al. 2006, in ESA Special Publication, Vol. 1306, The CoRoT Mission Pre-Launch Status - Stellar Seismology and Planet Finding, ed. M. Fridlund, A. Baglin, J. Lochard, & L. Conroy, 33

Ball, W. H., & Gizon, L. 2014, A&A, 568, A123

Ball, W. H., Themeßl, N., & Hekker, S. 2018, MNRAS, 478, 4697

Ball, W. H., Chaplin, W. J., Nielsen, M. B., et al. 2020, MNRAS, 499, 6084

Basu, S., Chaplin, W. J., & Elsworth, Y. 2010, ApJ, 710, 1596

Basu, S., & Kinnane, A. 2018, ApJ, 869, 8

Bertelli, G., Mateo, M., Chiosi, C., & Bressan, A. 1992, ApJ, 388, 400

Borucki, W. J., Koch, D., Basri, G., et al. 2010, Science, 327, 977

Bressan, A., Marigo, P., Girardi, L., et al. 2012, MNRAS, 427, 127

Campante, T. L., Corsaro, E., Lund, M. N., et al. 2019, ApJ, 885, 31

Chaplin, W. J., Serenelli, A. M., Miglio, A., et al. 2020, Nature Astronomy, 4, 382

Claret, A. 2007, A&A, 475, 1019

Claret, A., Giménez, A., Baroch, D., et al. 2021, A&A, 654, A17

Claret, A., & Torres, G. 2016, A&A, 592, A15

—. 2018, ApJ, 859, 100

—. 2019, ApJ, 876, 134

Constantino, T., & Baraffe, I. 2018, A&A, 618, A177

Costa, G., Girardi, L., Bressan, A., et al. 2019, MNRAS, 485, 4641

Cox, J. P., & Giuli, R. T. 1968, Principles of stellar structure

Cunha, M. S., Roxburgh, I. W., Aguirre Børsen-Koch, V., et al. 2021, MNRAS, 508, 5864

Deheuvels, S., Brandão, I., Silva Aguirre, V., et al. 2016, A&A, 589, A93

Deheuvels, S., & Michel, E. 2011, A&A, 535, A91

Demarque, P., Woo, J.-H., Kim, Y.-C., & Yi, S. K. 2004, ApJS, 155, 667

Gai, N., Basu, S., Chaplin, W. J., & Elsworth, Y. 2011, ApJ, 730, 63

Gaia Collaboration, Brown, A. G. A., Vallenari, A., et al. 2018, A&A, 616, A1

González-Cuesta, L., Mathur, S., García, R. A., et al. 2023, A&A, 674, A106

Grevesse, N., & Sauval, A. J. 1998, SSRv, 85, 161

Hekker, S., & Christensen-Dalsgaard, J. 2017, A&A Rv, 25, 1

Higl, J., Müller, E., & Weiss, A. 2021, A&A, 646, A133

Howell, S. B., Sobeck, C., Haas, M., et al. 2014, PASP, 126, 398

Huber, D., Chaplin, W. J., Chontos, A., et al. 2019, AJ, 157, 245

Jermyn, A. S., Bauer, E. B., Schwab, J., et al. 2023, ApJS, 265, 15

Jørgensen, A. C. S., Montalbán, J., Miglio, A., et al. 2020, MNRAS, 495, 4965

Li, T., Bedding, T. R., Christensen-Dalsgaard, J., et al. 2020a, MNRAS, 495, 3431

Li, Y., Bedding, T. R., Li, T., et al. 2020b, MNRAS, 495, 2363

Lindsay, C. J., Ong, J. M. J., & Basu, S. 2022, ApJ, 931, 116

—. 2023, ApJ, 950, 19

Lund, M. N., Silva Aguirre, V., Davies, G. R., et al. 2017, ApJ, 835, 172

Maeder, A., & Mermilliod, J. C. 1981, A&A, 93, 136

McKeever, J. M., Basu, S., & Corsaro, E. 2019, ApJ, 874, 180

Mombarg, J. S. G., Van Reeth, T., & Aerts, C. 2021, A&A, 650, A58

Mombarg, J. S. G., Van Reeth, T., Pedersen, M. G., et al. 2019, MNRAS, 485, 3248

Noll, A., & Deheuvels, S. 2023, arXiv e-prints, arXiv:2305.17176

Noll, A., Deheuvels, S., & Ballot, J. 2021, A&A, 647, A187

Nsamba, B., Moedas, N., Campante, T. L., et al. 2021, MNRAS, 500, 54

Ong, J. M. J., & Basu, S. 2020, ApJ, 898, 127

Ong, J. M. J., Basu, S., Lund, M. N., et al. 2021a, ApJ, 922, 18

Ong, J. M. J., Basu, S., & McKeever, J. M. 2021b, ApJ, 906, 54

Ong, J. M. J., Basu, S., & Roxburgh, I. W. 2021c, ApJ, 920, 8

Paxton, B., Bildsten, L., Dotter, A., et al. 2011, ApJS, 192, 3

Paxton, B., Cantiello, M., Arras, P., et al. 2013, ApJS, 208, 4

Paxton, B., Marchant, P., Schwab, J., et al. 2015, ApJS, 220, 15

Paxton, B., Schwab, J., Bauer, E. B., et al. 2018, ApJS, 234, 34

Paxton, B., Smolec, R., Schwab, J., et al. 2019, ApJS, 243, 10

Pietrinferni, A., Cassisi, S., Salaris, M., & Castelli, F. 2004, ApJ, 612, 168

Pols, O. R., Tout, C. A., Schroder, K.-P., Eggleton, P. P., & Manners, J. 1997, MNRAS, 289, 869

Reback, J., Mendel, J. B., McKinney, W., et al. 2021, pandas-dev/pandas: Pandas 1.3.0, v1.3.0, Zenodo, doi: 10.5281/zenodo.3509134

Ribas, I., Jordi, C., & Giménez, Á. 2000, MNRAS, 318, L55

Ricker, G. R., Winn, J. N., Vanderspek, R., et al. 2015, Journal of Astronomical Telescopes, Instruments, and Systems, 1, 014003

Rosenfield, P., Girardi, L., Williams, B. F., et al. 2017, ApJ, 841, 69

Schroder, K.-P., Pols, O. R., & Eggleton, P. P. 1997, MNRAS, 285, 696

Scuflaire, R. 1974, A&A, 36, 107

Serenelli, A., Johnson, J., Huber, D., et al. 2017, ApJS, 233, 23

Silva Aguirre, V., Lund, M. N., Antia, H. M., et al. 2017, ApJ, 835, 173

Steigman, G. 2010, JCAP, 2010, 029

Stello, D., Saunders, N., Grunblatt, S., et al. 2022, MNRAS, 512, 1677

Thoul, A. A., Bahcall, J. N., & Loeb, A. 1994, ApJ, 421, 828

Townsend, R. H. D., & Teitler, S. A. 2013, MNRAS, 435, 3406

VandenBerg, D. A., Bergbusch, P. A., & Dowler, P. D. 2006, ApJS, 162, 375

Viani, L. S., & Basu, S. 2020, ApJ, 904, 22

Viani, L. S., Basu, S., Ong J., M. J., Bonaca, A., & Chaplin, W. J. 2018, ApJ, 858, 28

Virtanen, P., Gommers, R., Oliphant, T. E., et al. 2020, Nature Methods, 17, 261

Yu, J., Huber, D., Bedding, T. R., et al. 2018, ApJS, 236, 42

Table 1. Modelling results for the subgiants in our sample observed by the *Kepler* and K2 missions.

Target	M [$M_\odot$]	R [$R_\odot$]	L [$L_\odot$]	$T_{\rm eff}$ [K]	Age [Gyr]	$[{\rm FeH}]_0$	Y_0	$\alpha_{\rm mlt}$	$\alpha_{\rm ov,\,eff}$
KIC2991448	$1.05^{+0.07}_{-0.06}$	$1.73^{+0.04}_{-0.03}$	$2.72^{+0.24}_{-0.18}$	5639^{+99}_{-78}	$8.21^{+0.93}_{-0.87}$	$-0.08^{+0.14}_{-0.13}$	$0.276^{+0.005}_{-0.005}$	$1.753^{+0.057}_{-0.041}$	$0.050^{+0.024}_{-0.050}$
KIC3852594	$1.19^{+0.07}_{-0.06}$	$2.01^{+0.04}_{-0.04}$	$5.59^{+0.33}_{-0.31}$	6270^{+66}_{-68}	$4.12^{+0.42}_{-0.38}$	$-0.31^{+0.13}_{-0.10}$	$0.275^{+0.006}_{-0.006}$	$1.972^{+0.026}_{-0.053}$	$0.069^{+0.005}_{-0.006}$
KIC4346201	$1.24^{+0.05}_{-0.06}$	$1.95^{+0.03}_{-0.03}$	$4.84^{+0.29}_{-0.32}$	6134^{+76}_{-85}	$4.31^{+0.49}_{-0.36}$	$-0.13^{+0.14}_{-0.11}$	$0.266^{+0.007}_{-0.006}$	$1.801^{+0.069}_{-0.045}$	$0.055^{+0.008}_{-0.005}$
KIC5108214	$1.50^{+0.07}_{-0.09}$	$2.57^{+0.04}_{-0.05}$	$6.96^{+0.40}_{-0.40}$	5855^{+72}_{-75}	$3.14^{+0.19}_{-0.17}$	$0.16^{+0.11}_{-0.14}$	$0.270^{+0.007}_{-0.007}$	$1.778^{+0.025}_{-0.024}$	$0.077^{+0.013}_{-0.009}$
KIC5607242	$1.25^{+0.09}_{-0.10}$	$2.43^{+0.06}_{-0.07}$	$4.85^{+0.38}_{-0.37}$	5500^{+82}_{-87}	$4.63^{+0.63}_{-0.47}$	$-0.11^{+0.15}_{-0.16}$	$0.274^{+0.006}_{-0.006}$	$1.789^{+0.011}_{-0.012}$	$0.126^{+0.016}_{-0.013}$
KIC5689820	$1.11^{+0.09}_{-0.07}$	$2.29^{+0.07}_{-0.05}$	$2.96^{+0.28}_{-0.22}$	5002^{+78}_{-70}	$8.69^{+1.07}_{-1.39}$	$0.09^{+0.11}_{-0.13}$	$0.281^{+0.004}_{-0.005}$	$1.837^{+0.050}_{-0.066}$	$0.107^{+0.028}_{-0.034}$
KIC5955122	$1.17^{+0.08}_{-0.08}$	$2.09^{+0.05}_{-0.05}$	$4.71^{+0.33}_{-0.37}$	5887^{+77}_{-86}	$5.03^{+0.69}_{-0.55}$	$-0.19^{+0.15}_{-0.16}$	$0.274^{+0.006}_{-0.005}$	$1.787^{+0.025}_{-0.029}$	$0.087^{+0.011}_{-0.012}$
KIC6064910	$1.28^{+0.06}_{-0.07}$	$2.31^{+0.04}_{-0.04}$	$7.41^{+0.42}_{-0.44}$	6272^{+73}_{-69}	$3.20^{+0.34}_{-0.28}$	$-0.24^{+0.12}_{-0.11}$	$0.287^{+0.005}_{-0.005}$	$1.890^{+0.046}_{-0.038}$	$0.101^{+0.015}_{-0.017}$
KIC6370489	$1.16^{+0.08}_{-0.08}$	$2.01^{+0.04}_{-0.05}$	$5.22^{+0.37}_{-0.35}$	6154^{+80}_{-77}	$4.47^{+0.60}_{-0.53}$	$-0.29^{+0.13}_{-0.14}$	$0.278^{+0.004}_{-0.005}$	$1.856^{+0.059}_{-0.040}$	$0.071^{+0.005}_{-0.009}$
KIC6442183	$0.98^{+0.04}_{-0.04}$	$1.64^{+0.02}_{-0.02}$	$2.55^{+0.19}_{-0.16}$	5697^{+90}_{-89}	$9.07^{+0.90}_{-0.84}$	$-0.18^{+0.11}_{-0.13}$	$0.278^{+0.003}_{-0.005}$	$1.775^{+0.059}_{-0.062}$	$0.000^{+0.033}_{-0.000}$
KIC6693861	$1.00^{+0.08}_{-0.06}$	$2.03^{+0.05}_{-0.04}$	$3.71^{+0.29}_{-0.27}$	5616^{+82}_{-79}	$7.22^{+1.02}_{-0.93}$	$-0.41^{+0.15}_{-0.13}$	$0.277^{+0.005}_{-0.005}$	$1.751^{+0.032}_{-0.019}$	$0.039^{+0.039}_{-0.039}$
KIC6766513	$1.30^{+0.06}_{-0.04}$	$2.10^{+0.04}_{-0.03}$	$5.91^{+0.31}_{-0.31}$	6203^{+71}_{-66}	$3.58^{+0.18}_{-0.19}$	$-0.10^{+0.10}_{-0.08}$	$0.275^{+0.007}_{-0.006}$	$1.830^{+0.082}_{-0.083}$	$0.061^{+0.005}_{-0.005}$
KIC7174707	$1.09^{+0.09}_{-0.07}$	$2.09^{+0.06}_{-0.05}$	$2.83^{+0.28}_{-0.24}$	5180^{+89}_{-84}	$8.31^{+1.17}_{-1.21}$	$0.02^{+0.14}_{-0.14}$	$0.277^{+0.004}_{-0.005}$	$1.797^{+0.021}_{-0.042}$	$0.097^{+0.029}_{-0.037}$
KIC7199397	$1.31^{+0.09}_{-0.07}$	$2.55^{+0.06}_{-0.05}$	$6.96^{+0.39}_{-0.38}$	5876^{+67}_{-64}	$3.46^{+0.31}_{-0.26}$	$-0.18^{+0.14}_{-0.13}$	$0.278^{+0.007}_{-0.007}$	$1.751^{+0.044}_{-0.023}$	$0.124^{+0.009}_{-0.014}$
KIC7668623	$1.56^{+0.04}_{-0.06}$	$2.39^{+0.02}_{-0.03}$	$8.08^{+0.26}_{-0.43}$	6297^{+46}_{-77}	$2.69^{+0.10}_{-0.05}$	$0.19^{+0.07}_{-0.10}$	$0.273^{+0.005}_{-0.006}$	$1.920^{+0.036}_{-0.042}$	$0.164^{+0.077}_{-0.084}$
KIC7747078	$1.10^{+0.07}_{-0.07}$	$1.94^{+0.05}_{-0.04}$	$4.07^{+0.31}_{-0.29}$	5894^{+82}_{-79}	$5.82^{+0.77}_{-0.66}$	$-0.25^{+0.15}_{-0.15}$	$0.278^{+0.006}_{-0.005}$	$1.767^{+0.051}_{-0.044}$	$0.070^{+0.021}_{-0.028}$
KIC7976303	$1.09^{+0.09}_{-0.07}$	$1.99^{+0.05}_{-0.04}$	$4.88^{+0.33}_{-0.34}$	6083^{+76}_{-76}	$5.14^{+0.68}_{-0.62}$	$-0.41^{+0.16}_{-0.13}$	$0.277^{+0.006}_{-0.006}$	$1.857^{+0.053}_{-0.046}$	$0.064^{+0.011}_{-0.025}$
KIC8026226	$1.47^{+0.07}_{-0.06}$	$2.87^{+0.05}_{-0.04}$	$10.99^{+0.45}_{-0.40}$	6206^{+63}_{-65}	$2.29^{+0.15}_{-0.10}$	$-0.21^{+0.14}_{-0.11}$	$0.272^{+0.007}_{-0.006}$	$1.796^{+0.020}_{-0.017}$	$0.083^{+0.011}_{-0.007}$
KIC8524425	$1.08^{+0.07}_{-0.06}$	$1.80^{+0.04}_{-0.03}$	$2.74^{+0.26}_{-0.21}$	5549^{+91}_{-85}	$8.01^{+0.97}_{-0.88}$	$0.02^{+0.12}_{-0.12}$	$0.279^{+0.005}_{-0.005}$	$1.743^{+0.037}_{-0.027}$	$0.071^{+0.028}_{-0.027}$
KIC8702606	$1.19^{+0.10}_{-0.10}$	$2.43^{+0.07}_{-0.07}$	$4.90^{+0.38}_{-0.38}$	5517^{+77}_{-84}	$4.83^{+0.80}_{-0.56}$	$-0.22^{+0.16}_{-0.17}$	$0.277^{+0.006}_{-0.006}$	$1.773^{+0.024}_{-0.020}$	$0.124^{+0.014}_{-0.028}$
KIC8738809	$1.40^{+0.06}_{-0.08}$	$2.21^{+0.03}_{-0.04}$	$5.86^{+0.35}_{-0.41}$	6055^{+66}_{-86}	$3.54^{+0.36}_{-0.26}$	$0.15^{+0.11}_{-0.14}$	$0.277^{+0.006}_{-0.006}$	$1.841^{+0.046}_{-0.041}$	$0.069^{+0.012}_{-0.011}$
KIC9512063	$1.10^{+0.09}_{-0.08}$	$2.03^{+0.06}_{-0.05}$	$4.26^{+0.36}_{-0.29}$	5819^{+86}_{-79}	$5.77^{+0.72}_{-0.70}$	$-0.28^{+0.18}_{-0.15}$	$0.278^{+0.005}_{-0.005}$	$1.796^{+0.047}_{-0.063}$	$0.076^{+0.028}_{-0.033}$
KIC10018963	$1.21^{+0.06}_{-0.08}$	$1.96^{+0.03}_{-0.04}$	$4.98^{+0.28}_{-0.32}$	6162^{+72}_{-70}	$4.36^{+0.58}_{-0.40}$	$-0.18^{+0.14}_{-0.14}$	$0.274^{+0.007}_{-0.006}$	$1.892^{+0.039}_{-0.042}$	$0.068^{+0.006}_{-0.006}$
KIC10147635	$1.47^{+0.08}_{-0.09}$	$2.71^{+0.05}_{-0.06}$	$8.31^{+0.44}_{-0.44}$	5954^{+71}_{-70}	$2.82^{+0.19}_{-0.10}$	$-0.03^{+0.15}_{-0.16}$	$0.271^{+0.007}_{-0.007}$	$1.790^{+0.042}_{-0.037}$	$0.105^{+0.021}_{-0.011}$
KIC10273246	$1.40^{+0.06}_{-0.06}$	$2.25^{+0.03}_{-0.04}$	$6.31^{+0.36}_{-0.36}$	6106^{+91}_{-75}	$3.33^{+0.28}_{-0.25}$	$0.10^{+0.12}_{-0.12}$	$0.278^{+0.005}_{-0.005}$	$1.854^{+0.019}_{-0.023}$	$0.067^{+0.010}_{-0.016}$
KIC10593351	$1.62^{+0.08}_{-0.10}$	$3.16^{+0.06}_{-0.07}$	$9.84^{+0.46}_{-0.42}$	5764^{+71}_{-65}	$2.45^{+0.18}_{-0.14}$	$0.12^{+0.13}_{-0.19}$	$0.274^{+0.005}_{-0.006}$	$1.767^{+0.028}_{-0.031}$	$0.135^{+0.050}_{-0.021}$
KIC10873176	$1.12^{+0.06}_{-0.05}$	$2.05^{+0.04}_{-0.03}$	$5.98^{+0.35}_{-0.39}$	6294^{+72}_{-71}	$4.04^{+0.53}_{-0.40}$	$-0.41^{+0.12}_{-0.10}$	$0.297^{+0.007}_{-0.005}$	$1.999^{+0.053}_{-0.043}$	$0.082^{+0.013}_{-0.021}$
KIC10920273	$1.00^{+0.05}_{-0.04}$	$1.79^{+0.03}_{-0.02}$	$2.47^{+0.21}_{-0.18}$	5415^{+86}_{-95}	$9.70^{+0.81}_{-0.90}$	$-0.10^{+0.09}_{-0.10}$	$0.273^{+0.004}_{-0.004}$	$1.696^{+0.070}_{-0.067}$	$0.000^{+0.064}_{-0.000}$
KIC10972873	$1.06^{+0.08}_{-0.06}$	$1.80^{+0.05}_{-0.04}$	$3.08^{+0.25}_{-0.24}$	5694^{+85}_{-95}	$7.50^{+0.94}_{-0.89}$	$-0.12^{+0.15}_{-0.14}$	$0.277^{+0.004}_{-0.005}$	$1.797^{+0.036}_{-0.040}$	$0.054^{+0.017}_{-0.054}$
KIC11026764	$1.09^{+0.10}_{-0.08}$	$2.01^{+0.06}_{-0.05}$	$3.48^{+0.30}_{-0.26}$	5553^{+84}_{-75}	$6.69^{+0.94}_{-0.81}$	$-0.11^{+0.17}_{-0.16}$	$0.286^{+0.005}_{-0.005}$	$1.796^{+0.023}_{-0.028}$	$0.087^{+0.028}_{-0.040}$
KIC11137075	$0.98^{+0.05}_{-0.04}$	$1.63^{+0.03}_{-0.02}$	$2.22^{+0.17}_{-0.16}$	5513^{+91}_{-92}	$10.27^{+0.94}_{-1.04}$	$-0.08^{+0.11}_{-0.12}$	$0.279^{+0.003}_{-0.004}$	$1.699^{+0.054}_{-0.062}$	$0.000^{+0.046}_{-0.000}$
KIC11193681	$1.39^{+0.07}_{-0.09}$	$2.44^{+0.04}_{-0.06}$	$5.10^{+0.37}_{-0.33}$	5558^{+86}_{-76}	$4.13^{+0.34}_{-0.24}$	$0.16^{+0.12}_{-0.16}$	$0.273^{+0.005}_{-0.005}$	$1.772^{+0.031}_{-0.025}$	$0.119^{+0.011}_{-0.013}$
KIC11395018	$1.22^{+0.08}_{-0.08}$	$2.16^{+0.05}_{-0.05}$	$4.49^{+0.35}_{-0.34}$	5720^{+94}_{-90}	$5.04^{+0.63}_{-0.52}$	$-0.04^{+0.16}_{-0.15}$	$0.278^{+0.007}_{-0.007}$	$1.824^{+0.044}_{-0.041}$	$0.113^{+0.008}_{-0.010}$
KIC11414712	$1.16^{+0.13}_{-0.11}$	$2.25^{+0.08}_{-0.08}$	$4.49^{+0.52}_{-0.47}$	5599^{+99}_{-95}	$5.40^{+1.16}_{-0.86}$	$-0.20^{+0.20}_{-0.19}$	$0.277^{+0.001}_{-0.002}$	$1.770^{+0.021}_{-0.014}$	$0.099^{+0.017}_{-0.037}$
KIC11771760	$1.56^{+0.10}_{-0.09}$	$3.05^{+0.07}_{-0.06}$	$9.92^{+0.41}_{-0.43}$	5864^{+69}_{-70}	$2.38^{+0.09}_{-0.06}$	$-0.05^{+0.18}_{-0.15}$	$0.265^{+0.007}_{-0.006}$	$1.776^{+0.028}_{-0.032}$	$0.096^{+0.008}_{-0.011}$
KIC12508433	$1.25^{+0.09}_{-0.10}$	$2.27^{+0.06}_{-0.07}$	$3.63^{+0.32}_{-0.31}$	5295^{+89}_{-82}	$5.93^{+0.91}_{-0.63}$	$0.13^{+0.13}_{-0.16}$	$0.277^{+0.005}_{-0.006}$	$1.770^{+0.033}_{-0.026}$	$0.131^{+0.009}_{-0.014}$
EPIC212478598	$0.98^{+0.05}_{-0.04}$	$2.44^{+0.04}_{-0.03}$	$3.55^{+0.25}_{-0.23}$	5081^{+86}_{-89}	$9.22^{+0.53}_{-0.66}$	$-0.32^{+0.12}_{-0.13}$	$0.275^{+0.004}_{-0.004}$	$1.745^{+0.113}_{-0.122}$	$0.000^{+0.055}_{-0.000}$
EPIC212516207	$1.19^{+0.18}_{-0.05}$	$1.70^{+0.07}_{-0.02}$	$3.78^{+0.26}_{-0.18}$	6165^{+42}_{-40}	$4.84^{+0.38}_{-0.98}$	$-0.01^{+0.19}_{-0.11}$	$0.279^{+0.008}_{-0.011}$	$2.018^{+0.021}_{-0.042}$	$0.073^{+0.017}_{-0.009}$
EPIC212586030	$1.13^{+0.11}_{-0.08}$	$3.51^{+0.12}_{-0.09}$	$6.14^{+0.40}_{-0.36}$	4851^{+64}_{-63}	$8.33^{+1.25}_{-1.52}$	$0.07^{+0.11}_{-0.14}$	$0.280^{+0.005}_{-0.004}$	$1.872^{+0.090}_{-0.120}$	$0.122^{+0.020}_{-0.036}$
EPIC212683142	$1.28^{+0.09}_{-0.09}$	$2.27^{+0.05}_{-0.05}$	$5.56^{+0.36}_{-0.37}$	5885^{+85}_{-77}	$4.14^{+0.44}_{-0.37}$	$-0.09^{+0.17}_{-0.16}$	$0.272^{+0.006}_{-0.006}$	$1.866^{+0.068}_{-0.063}$	$0.088^{+0.020}_{-0.009}$
EPIC246154489	$1.12^{+0.10}_{-0.08}$	$4.65^{+0.15}_{-0.13}$	$12.32^{+0.49}_{-0.46}$	5017^{+64}_{-70}	$5.85^{+1.12}_{-1.14}$	$-0.43^{+0.15}_{-0.12}$	$0.274^{+0.004}_{-0.002}$	$1.808^{+0.109}_{-0.129}$	$0.118^{+0.021}_{-0.038}$
EPIC246184564	$1.33^{+0.09}_{-0.10}$	$5.62^{+0.15}_{-0.16}$	$16.88^{+0.48}_{-0.47}$	4941^{+66}_{-63}	$3.87^{+0.71}_{-0.64}$	$-0.24^{+0.13}_{-0.15}$	$0.273^{+0.004}_{-0.003}$	$1.833^{+0.105}_{-0.132}$	$0.147^{+0.012}_{-0.013}$
EPIC246305274	$1.17^{+0.12}_{-0.09}$	$2.15^{+0.07}_{-0.05}$	$5.90^{+0.69}_{-0.54}$	6146^{+97}_{-97}	$4.19^{+0.71}_{-0.69}$	$-0.34^{+0.17}_{-0.15}$	$0.282^{+0.003}_{-0.004}$	$1.846^{+0.027}_{-0.043}$	$0.069^{+0.007}_{-0.021}$
EPIC246305350	$1.31^{+0.09}_{-0.05}$	$2.21^{+0.05}_{-0.03}$	$5.68^{+0.33}_{-0.35}$	5999^{+72}_{-88}	$3.87^{+0.26}_{-0.24}$	$-0.03^{+0.16}_{-0.09}$	$0.271^{+0.008}_{-0.006}$	$1.741^{+0.113}_{-0.084}$	$0.081^{+0.008}_{-0.006}$

Table 2. Modelling results for the subgiants in our sample observed by the TESS mission.

Target	M [$M_\odot$]	R [$R_\odot$]	L [$L_\odot$]	$T_{\rm eff}$ [K]	Age [Gyr]	$[\rm FeH]_0$	Y_0	$\alpha_{\rm mlt}$	$\alpha_{\rm ov,\,eff}$
HD 38529	$1.48^{+0.07}_{-0.09}$	$2.68^{+0.10}_{-0.08}$	$6.24^{+0.38}_{-0.42}$	5564^{+83}_{-93}	$3.30^{+0.24}_{-0.19}$	$0.20^{+0.13}_{-0.17}$	$0.281^{+0.003}_{-0.003}$	$1.782^{+0.014}_{-0.017}$	$0.109^{+0.008}_{-0.013}$
ν Ind	$0.89^{+0.04}_{-0.03}$	$2.94^{+0.04}_{-0.03}$	$6.11^{+0.36}_{-0.32}$	5298^{+61}_{-66}	$8.63^{+0.73}_{-0.96}$	$-0.89^{+0.05}_{-0.03}$	$0.274^{+0.003}_{-0.004}$	$1.745^{+0.101}_{-0.104}$	$0.000^{+0.000}_{-0.000}$
δ Eri	$1.08^{+0.07}_{-0.06}$	$2.29^{+0.05}_{-0.04}$	$2.85^{+0.26}_{-0.22}$	4958^{+82}_{-82}	$9.11^{+0.81}_{-1.06}$	$0.02^{+0.12}_{-0.14}$	$0.278^{+0.003}_{-0.004}$	$1.731^{+0.077}_{-0.095}$	$0.080^{+0.027}_{-0.027}$
β Hyi	$1.08^{+0.09}_{-0.07}$	$1.82^{+0.05}_{-0.04}$	$3.49^{+0.29}_{-0.26}$	5849^{+81}_{-81}	$6.46^{+0.84}_{-0.81}$	$-0.16^{+0.17}_{-0.15}$	$0.281^{+0.005}_{-0.005}$	$1.799^{+0.061}_{-0.061}$	$0.057^{+0.019}_{-0.024}$
η Cep	$1.02^{+0.08}_{-0.06}$	$3.94^{+0.11}_{-0.09}$	$8.21^{+0.40}_{-0.38}$	4917^{+71}_{-65}	$8.97^{+0.89}_{-1.18}$	$-0.22^{+0.16}_{-0.14}$	$0.279^{+0.004}_{-0.004}$	$1.843^{+0.100}_{-0.128}$	$0.056^{+0.035}_{-0.056}$
TOI 197	$1.12^{+0.13}_{-0.10}$	$2.91^{+0.11}_{-0.09}$	$5.01^{+0.42}_{-0.35}$	5064^{+72}_{-75}	$6.82^{+1.36}_{-1.57}$	$-0.18^{+0.15}_{-0.15}$	$0.277^{+0.005}_{-0.005}$	$1.873^{+0.081}_{-0.106}$	$0.082^{+0.016}_{-0.031}$
TIC300088321	$1.05^{+0.05}_{-0.05}$	$1.67^{+0.03}_{-0.03}$	$2.41^{+0.19}_{-0.17}$	5568^{+90}_{-83}	$8.76^{+1.05}_{-0.88}$	$0.03^{+0.11}_{-0.12}$	$0.283^{+0.004}_{-0.004}$	$1.728^{+0.044}_{-0.038}$	$0.055^{+0.025}_{-0.055}$
TIC29987134	$1.25^{+0.11}_{-0.11}$	$2.26^{+0.07}_{-0.07}$	$5.45^{+0.53}_{-0.50}$	5876^{+93}_{-94}	$4.25^{+0.72}_{-0.54}$	$-0.12^{+0.18}_{-0.18}$	$0.277^{+0.003}_{-0.002}$	$1.749^{+0.022}_{-0.014}$	$0.088^{+0.009}_{-0.012}$
TIC374858999	$1.12^{+0.15}_{-0.11}$	$2.90^{+0.13}_{-0.10}$	$5.59^{+0.42}_{-0.41}$	5210^{+90}_{-95}	$5.69^{+1.42}_{-1.34}$	$-0.45^{+0.22}_{-0.18}$	$0.271^{+0.004}_{-0.004}$	$1.785^{+0.065}_{-0.076}$	$0.082^{+0.022}_{-0.036}$
TIC349059821	$1.04^{+0.11}_{-0.07}$	$2.91^{+0.10}_{-0.07}$	$5.05^{+0.39}_{-0.34}$	5071^{+73}_{-76}	$7.52^{+1.15}_{-1.45}$	$-0.34^{+0.15}_{-0.15}$	$0.275^{+0.005}_{-0.005}$	$1.770^{+0.108}_{-0.118}$	$0.064^{+0.035}_{-0.064}$
TIC55270123	$1.13^{+0.14}_{-0.11}$	$3.09^{+0.13}_{-0.10}$	$5.59^{+0.47}_{-0.39}$	5054^{+79}_{-82}	$6.49^{+1.46}_{-1.56}$	$-0.21^{+0.16}_{-0.16}$	$0.274^{+0.005}_{-0.005}$	$1.858^{+0.085}_{-0.109}$	$0.086^{+0.015}_{-0.032}$
TIC167548586	$1.26^{+0.12}_{-0.12}$	$3.24^{+0.11}_{-0.12}$	$5.68^{+0.45}_{-0.41}$	4954^{+76}_{-73}	$5.54^{+1.49}_{-1.20}$	$-0.02^{+0.14}_{-0.16}$	$0.274^{+0.004}_{-0.004}$	$1.817^{+0.095}_{-0.114}$	$0.116^{+0.010}_{-0.017}$
TIC299899690	$1.25^{+0.15}_{-0.13}$	$3.52^{+0.16}_{-0.15}$	$7.89^{+0.95}_{-0.83}$	5164^{+85}_{-85}	$4.57^{+1.46}_{-1.25}$	$-0.31^{+0.15}_{-0.16}$	$0.275^{+0.004}_{-0.004}$	$1.870^{+0.066}_{-0.094}$	$0.106^{+0.016}_{-0.020}$
TIC350343922	$1.04^{+0.10}_{-0.07}$	$3.67^{+0.12}_{-0.09}$	$7.77^{+0.55}_{-0.47}$	5031^{+66}_{-73}	$7.95^{+1.13}_{-1.48}$	$-0.29^{+0.14}_{-0.12}$	$0.280^{+0.004}_{-0.004}$	$1.895^{+0.085}_{-0.121}$	$0.074^{+0.040}_{-0.074}$
TIC150442152	$1.28^{+0.11}_{-0.12}$	$4.14^{+0.13}_{-0.14}$	$9.19^{+0.47}_{-0.45}$	4948^{+70}_{-69}	$5.18^{+1.26}_{-0.98}$	$-0.04^{+0.15}_{-0.16}$	$0.277^{+0.004}_{-0.004}$	$1.918^{+0.074}_{-0.111}$	$0.116^{+0.010}_{-0.014}$
TIC150166759	$1.07^{+0.09}_{-0.07}$	$4.21^{+0.13}_{-0.11}$	$8.80^{+0.51}_{-0.50}$	4842^{+70}_{-68}	$8.69^{+0.95}_{-1.21}$	$-0.11^{+0.15}_{-0.16}$	$0.279^{+0.004}_{-0.004}$	$1.815^{+0.110}_{-0.130}$	$0.093^{+0.034}_{-0.040}$
TIC141757732	$1.28^{+0.11}_{-0.11}$	$5.40^{+0.18}_{-0.17}$	$16.84^{+0.61}_{-0.58}$	5035^{+74}_{-76}	$3.89^{+0.85}_{-0.68}$	$-0.41^{+0.16}_{-0.16}$	$0.274^{+0.003}_{-0.003}$	$1.825^{+0.103}_{-0.129}$	$0.141^{+0.011}_{-0.015}$
TIC350335258	$1.13^{+0.10}_{-0.08}$	$5.79^{+0.20}_{-0.19}$	$17.54^{+0.77}_{-0.76}$	4911^{+75}_{-74}	$5.20^{+1.05}_{-0.92}$	$-0.57^{+0.17}_{-0.15}$	$0.274^{+0.002}_{-0.002}$	$1.621^{+0.131}_{-0.111}$	$0.137^{+0.026}_{-0.050}$